

Inclusive charged-hadron production in 100–400-GeV p - p collisions

J. R. Johnson,* R. Kammerud,† T. Ohsugi, D. J. Ritchie, R. Shafer, D. Theriot, and J. K. Walker
Fermi National Accelerator Laboratory, Batavia, Illinois 60510

F. E. Taylor

Northern Illinois University, DeKalb, Illinois 60115

(Received 3 October 1977)

Measurements have been made on the single-particle inclusive reactions $p + p \rightarrow \pi^\pm, K^\pm, p$, or \bar{p} + anything at 100, 200, and 400 GeV incident proton energies at Fermilab. The data cover a wide range in the radial scaling variable x_R ($0.05 \leq x_R \leq 1.0$) in the low- p_\perp region ($0.25 \leq p_\perp \leq 1.5$ GeV/ c). The x_R and p_\perp distributions are presented. The π^+/π^- , K^+/K^- , and π^\pm/K^\pm ratios are shown and are compared with data at higher p_\perp . The experimental techniques and the data analysis procedures are described in detail.

INTRODUCTION

Single-particle inclusive reactions in high-energy hadron-hadron collisions are of major experimental and theoretical interest. This interest is derived from the hope that at high p_\perp , the quark-parton model, which has been so successful in high-energy lepton-hadron scattering, may be applied to pure hadron scattering. In terms of the quark-parton model, inclusive hadron production at large p_\perp may be used to probe the constituent structure of the colliding hadrons and of the detected hadron.

The understanding of single-particle inclusive cross sections has been slow, primarily because the observed p_\perp dependence does not agree with dimensional arguments of the quark-parton model at currently available energies. Various mechanisms, based for example on quark-quark elastic scattering¹ or on constituent interchange,² have been proposed to explain the experimental results. These models are generally limited to the large- p_\perp region where the hard scattering of the initial projectiles is supposed to reveal a simple underlying structure.

A complete understanding of inclusive reactions must cover the entire kinematic region and hence must include the low- p_\perp region as well as the high- p_\perp region. In the low- p_\perp region we expect hadrons to be produced by low- p_\perp quarks fragmenting from the initial colliding hadrons. This hadron-production mechanism is a long-range process. High- p_\perp hadron production, on the other hand, must be a short-range process. Therefore, it is of interest to compare the p_\perp and x_R dependences for various secondary particles in these two kinematic regions. Of particular interest is to compare the particle ratios π^+/π^- , K^+/K^- , π^\pm/K^\pm in these two kinematic regions since this would allow interesting small differences of the cross sections to be seen.³

The invariant cross section for single-particle inclusive production $E(d\sigma/dp^3)(p + p \rightarrow h + X)$ may be written as a function of three variables p_\perp , $x_R = E^*/E^*_{\max}$, and the c.m. energy squared, s . We have previously used the radial scaling variable x_R in the analysis of an experiment performed at Fermilab on single- π^0 inclusive production⁴ as well as in an analysis of an extensive compilation of inclusive hadron data.⁵ The invariant cross sections in terms of x_R show a simple scaling behavior over a wide kinematic range. This scaling range appears to be wider when x_R is used than when Feynman $x = 2p_\perp/\sqrt{s}$ is used. It is therefore worthwhile to measure the invariant cross section by systematically holding two of these three variables constant while varying the third. It is hoped that in this way, certain simplicities will be evident and detailed questions such as radial scaling, the p_\perp and x_R dependencies may be measured without model-dependent assumptions.

The data presented here were taken in the low- p_\perp region, $0.25 \leq p_\perp \leq 1.5$ GeV/ c , for incident proton energies of 100, 200, and 400 GeV for the reactions $p + p \rightarrow h + X$ where $h = \pi^\pm, K^\pm, p$, or \bar{p} . The invariant cross sections for fixed p_\perp and s were measured versus x_R in the range $0.05 \leq x_R \leq 1.0$ corresponding to roughly 126° to 177° in the c.m. frame.

EXPERIMENTAL SETUP

The experiment was conducted in the P-West pit area of the Proton Laboratory of Fermi National Accelerator Laboratory. A well collimated primary proton beam was allowed to traverse a 13-cm liquid-hydrogen target. The produced particles were detected by a set of scintillation and Čerenkov counters in a 2.4-GeV/ c spectrometer made from two half quadrupole magnets. A system of proportional wire chambers was used

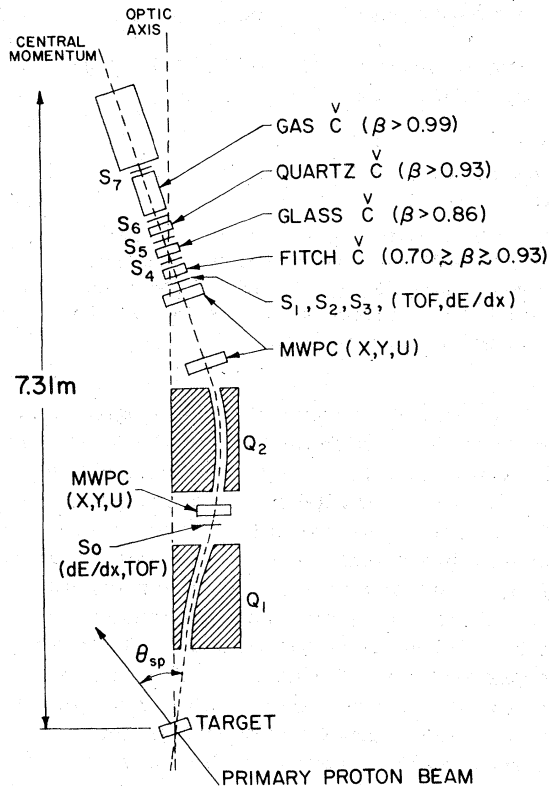


FIG. 1. The apparatus is shown in plan view. The central momentum trajectory is the dotted line through the two half quadrupoles Q_1 and Q_2 . Scintillation counters are denoted by S_i , $i = 0, 1, \dots, 7$, multiwire proportional chambers by MWPC, and Čerenkov counters by \bar{C} .

to achieve good momentum resolution and to define the acceptance of the spectrometer. The momentum acceptance was $\Delta p/p \approx \pm 10\%$ and the solid angle acceptance $\Delta\Omega \approx 2 \times 10^{-4}$ sr. This modest low-momentum spectrometer covered a large kinematic range by detecting slow particles in the lab frame which were produced in the backward hemisphere in the c.m. frame. The absolute normalizations of the particle yields were made by calibrated secondary-emission monitors to measure the incident proton flux and a detailed Monte Carlo study of the spectrometer acceptance. Figure 1 provides an overview of the apparatus.

A. The spectrometer

The half quadrupoles used in the spectrometer were obtained from splitting the quadrupole Deir-

dre at the Cambridge Electron Accelerator (CEA).⁶ A 15.24-cm-thick soft iron plate was used to image the half quadrupole field making the resulting field look like a full quadrupole field with half the full quadrupole aperture. Each half quadrupole of the spectrometer was 121.92 cm long with 15.24-cm radius pole tips. The half quadrupoles were separated by 60.96 cm and were mounted on a remotely moveable spectrometer arm which could be rotated from 5° to 125° in the lab.

The spectrometer was constructed so that the first quadrupole focused in the vertical plane and the second magnet focused in the horizontal plane. The optics from this arrangement resulted in rays in the vertical plane being focused from point to parallel, and in the horizontal plane from parallel to point.

Detailed ray-tracing calculations of the magnet were performed by three independent methods: (1) by a model of Collins,⁷ (2) by using the first- and second-order transfer matrices in the program TRANSPORT,⁸ including approximations to the fringe fields, and (3) by a model which divided the quadrupole fields into short pure quadrupole fields. The 12-pole components were included in this last calculation and were found to have a negligible effect. The shape of the fringe field was taken from measurements performed at the CEA⁶ and were checked on the half-quadrupole configuration used in this spectrometer by a calibrated Rawson probe. The current excitation of the spectrometer magnets was measured by a transducer calibrated by a precision shunt. In addition, a current digitizer using a precision shunt was read out at each beam spill, allowing checks of the short-term stability to be made.

Checks of the absolute momentum calibration of the spectrometer were performed by using the known kinematics of p - p elastic scattering and by using the time-of-flight (TOF) of low-momentum protons. These tests showed that the absolute momentum calibration was known to $\Delta p/p = \pm 2\%$.

The entire lengths of both quadrupoles were filled with lead collimators cut to always be ~ 2 cm larger than the envelope of rays defined by the multiwire proportional chamber (MWPC) acceptance. This lead made direct sight between the detectors and the target impossible, thereby allowing the spectrometer to operate at high beam intensities. Helium bags were placed inside each magnet aperture to reduce multiple scattering and nuclear absorption. The regions between the two quadrupoles and the end of the second quadrupole were completely enclosed by 15-cm-thick steel plates to shield the MWPC's and counters against room background radiation.

B. The multiwire proportional chambers

Nine multiwire proportional wire chambers were employed to give a set of x - y - u coordinates (x is vertical, y is horizontal, u is 45° diagonal) at three locations along the trajectory of the detected particles. (See Fig. 1.) These chambers allowed the momentum of the detected particle to be determined to $\pm 2\%$ over the $\pm 10\%$ acceptance of the spectrometer. Each MWPC consisted of 64 sense wires separated by 1 mm. The cathode planes were made from 5-mil aluminum foil. A gas mixture consisting of 80% Ar, 20% CO_2 was used.

Each chamber plane provided the multiplicity of hits and the positions of the first three hits. Since only single tracks were of interest, this number of digitized coordinates per plane was sufficient. The track-reconstruction efficiency was typically better than 95% for events with an identifiable particle species. Each event was digitized and read through a CAMAC system to an on-line PDP-11 computer. A fast OR pulse from each chamber plane was used to monitor chamber operation and was employed in the event trigger to reduce accidentals.

C. The counter system

Seven scintillation and four Čerenkov counters comprised the basic counter system of the 2.4-GeV/ c spectrometer. The locations of these counters are shown in Fig. 1. The event trigger which initiated the computer read-out process was generated by the $S_0 \cdot S_1 \cdot S_2 \cdot S_3 \cdot \text{FOML}$ coincidence, where FOML is the output of the fast OR majority logic of the MWPC's. This fast OR logic provided a 100-nsec-wide pulse each time a particle traversed the MWPC system. The use of the FOML signal significantly reduced the accidentals in the event trigger so that even at the highest beam intensities (2×10^{11} protons/sec) there were less than 10% accidental triggers.

To collect data on the rare particles K^- and \bar{p} , a special trigger was used to prescale the more copiously produced negative pions. This trigger involved identifying the π^- mesons by the scintillation and Čerenkov counters and prescaling them into the event trigger.

All the scintillation and Čerenkov counters were pulse-height-analyzed and latched through the CAMAC system. The TOF between S_0 and S_1 was digitized and recorded for each event. All events were written on magnetic tape for later off-line data analysis. Various checks of MWPC performances and counter pulse-height stability were performed on-line during the data collection. All important counter and coincidence rates were

recorded at the end of each beam spill and at the end of each data run.

A brief description of the counters employed in the spectrometer is as follows. The scintillation counters were made from a Pilot B scintillator

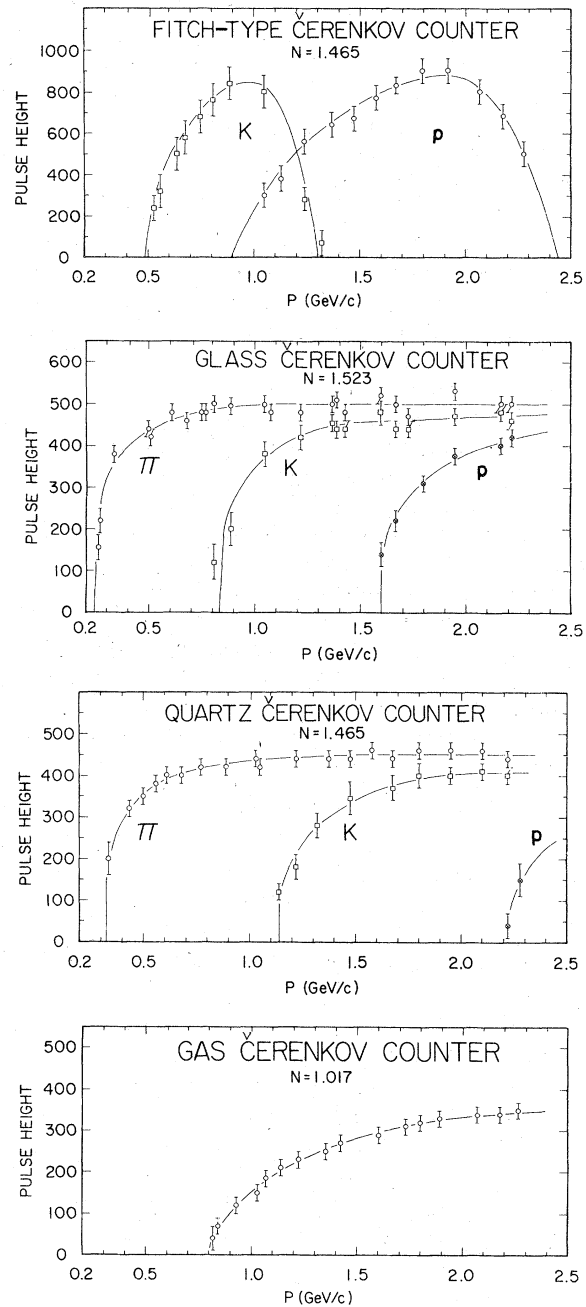


FIG. 2. The empirically determined responses of the four Čerenkov counters are shown as a function of the spectrometer momentum. The lines through the data are to guide the eye.

TABLE I. The parameters of the four Čerenkov counters are tabulated.

| Counter | Refractive index | Effective β threshold | Momentum at effective threshold (GeV/c) | | | | | Effective β cutoff | Momentum of cutoff (GeV/c) | | | | |
|---------|------------------|-----------------------------|---|-------|-------|------|------|--------------------------|----------------------------|-------|-------|-----|-----|
| | | | e | μ | π | K | p | | e | μ | π | K | p |
| Fitch | 1.465 | 0.68 | 0.0005 | 0.10 | 0.13 | 0.46 | 0.87 | 0.93 | 0.0014 | 0.29 | 0.35 | 1.4 | 2.6 |
| Glass | 1.523 | 0.87 | 0.0009 | 0.18 | 0.24 | 0.83 | 1.6 | ... | ... | ... | ... | ... | |
| Quartz | 1.465 | 0.93 | 0.0013 | 0.27 | 0.35 | 1.2 | 2.5 | ... | ... | ... | ... | ... | |
| Gas | 1.017 | 0.98 | 0.0026 | 0.57 | 0.75 | 2.7 | 5.0 | ... | ... | ... | ... | ... | |

in thicknesses ranging from 1.59 mm to 6.35 mm. The four Čerenkov counters were (1) a Fitch-type counter made from fused quartz; this counter furnished both a lower as well as an upper threshold, (2) a critical internal reflection counter made from glass, (3) a critical internal reflection counter made from quartz, and (4) a gas Čerenkov counter using Freon-13 at 20.3-(kg/cm²) pressure. The details of these Čerenkov counters⁹ are summarized in Table I.

The response of the counter system to different particle species was studied by first separating the easily identifiable protons by a dE/dX cut on S_0 and a TOF cut. The remaining pions and kaons could be separated by cuts in the Čerenkov counters. The Čerenkov-counter responses determined by this analysis are shown in Fig. 2. The Fitch, glass, and quartz counters had efficiencies $\approx 97\%$ over their respective momentum ranges. The gas counter efficiency was greater than 99%. The TOF response for identified particles is shown in Fig. 3 where $(1/\beta^2 - 1)$ determined from the TOF is plotted versus $1/p^2$. The

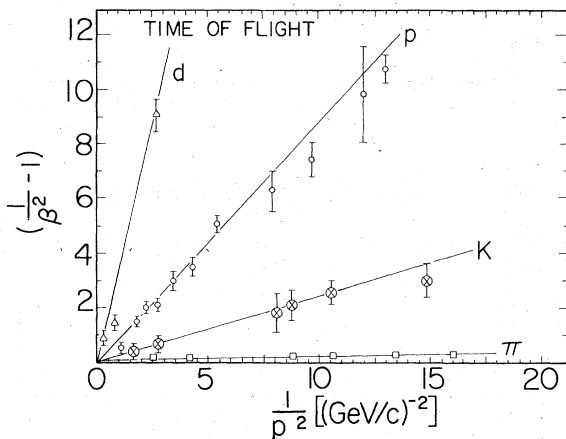


FIG. 3. The value of $(1/\beta^2 - 1)$ determined by the TOF between S_0 and S_1 is plotted versus $1/p^2$ where p is the central momentum of the spectrometer. A given particle species falls on a unique line.

expected straight-line correlations for a given particle species are evident.

D. The liquid-hydrogen target

The liquid-hydrogen target was made 13 cm long and 12 cm in diameter and could be both rotated horizontally and translated vertically. Data were taken with the target axis rotated by one half the lab angle of the spectrometer to minimize multiple scattering and nuclear interactions of the detected secondary particles. The vertical mobility of the target was useful in studying backgrounds and in minimizing the radiation damage of the target windows. The large target size placed the target windows outside the spectrometer acceptance for most running conditions, making the empty-target background subtractions small.

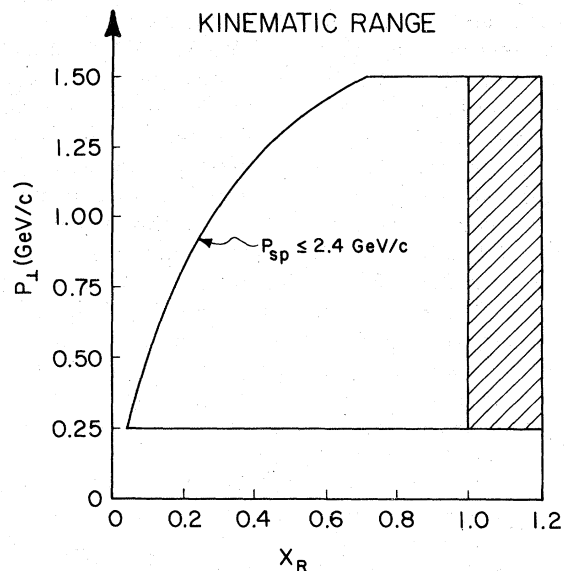


FIG. 4. The kinematic range in p_1 and x_R covered by the 2.4-GeV/c spectrometer. The left-hand boundary is determined by the maximum momentum of the spectrometer. Data were taken beyond the kinematic boundary $x_R=1$, shown in the cross-hatched region, to check background rates.

DATA COLLECTION

The data were collected by holding the transverse momentum p_{\perp} constant and sweeping through the scaling variable x_R at a given incident beam energy. These sweeps were performed by changing both the lab angle and the momentum of the spectrometer. Both positive and negative polarities were measured at a given spectrometer momentum and angle setting. The data at 400 GeV incident proton energy were taken during a standard 400-GeV machine flat-top operation, and the data at 100 and 200 GeV were taken during a special operation of the accelerator at a 200-GeV flat top with beam also extracted at a 100-GeV front porch. The kinematic range of the experiment is shown in Fig. 4. This kinematic range corresponds to roughly 126° to 177° in the c.m. frame and is therefore in the target-fragmentation region. Empty-target runs were only taken at 400 GeV incident energy. The empty-target contribution to the particle yields was typically less than 5% for $x_R \leq 0.75$ and somewhat greater for higher x_R .

DATA REDUCTION

The various stages of the data reduction were performed at the Fermilab Computer Facility. The raw data tapes were read on the CDC 6600 using the histogram program KIOWA¹⁰ to determine the number of particles of a given species and to reconstruct the momentum and target-position distributions. The results of this analysis were then written on a summary tape which was read by the PDP-10 computer to calculate the normal-

ized invariant cross sections.

The particle identification was performed by making appropriate cuts on the TOF, dE/dX , and four Čerenkov-counter pulse heights. These cuts were a function of the spectrometer momentum and are summarized in Table II. For the rare particles K^{\pm} and \bar{p} , a detailed examination of the various histograms was necessary to sufficiently refine the sample of events so that the invariant cross section could be calculated.

The momentum reconstruction was performed by using the first- and second-order matrices of the double-quadrupole-magnet spectrometer determined by the program TRANSPORT⁹ and the position information furnished by the MWPC's. The track reconstruction efficiency was $\geq 85\%$ for raw events and $\geq 95\%$ for events with an identifiable particle species. Cuts on the $\Delta p/p$, target position, and angle distributions were made to eliminate bad events. To ensure that the particle passed through the Čerenkov counters, appropriate cuts on the calculated projection of the particle trajectory on the S_7 counter were made (see Fig. 1). These cuts reduced the number of accepted events by 40% and served as the primary aperture cut.

The normalized invariant cross sections were calculated by

$$\frac{E}{p^2} \frac{d\sigma}{dpd\Omega} = \frac{E}{p^3} \frac{N_e \eta}{[(\Delta p/p) \Delta \cos\theta \Delta\phi \Delta Z_B N_B] \rho}, \quad (1)$$

where N_e = the number of detected particles with a given identifiable particle species having a reconstructed track, E = total energy of particle at p = central momentum of the spectrometer,

TABLE II. The details of the particle-identification algorithm are shown. The overline is used to denote the veto condition. For example, to identify K^{\pm} for $0.781 \leq p \leq 0.90$ GeV/c, the condition: Fitch \check{C} quartz \check{C} and a TOF cut are required.

| P_{τ} (GeV/c) | 0.384 | 0.548 | 0.702 | 1.20 | | | | |
|--------------------|----------------|-------------------------------------|---|--|---|--|--|--|
| π^{\pm} | TOF dE/dX | TOF glass \check{C} dE/dX | glass \check{C} quartz \check{C} | glass \check{C} quartz \check{C} Fitch \check{C} | | | gas \check{C} quartz \check{C} | |
| P_K (GeV/c) | 0.439 | | 0.658 | 0.781 | 0.90 | 1.06 | 1.20 | 1.53 |
| K^{\pm} | TOF dE/dX | TOF glass \check{C} | Fitch \check{C} TOF glass \check{C} | Fitch \check{C} TOF quartz \check{C} | Fitch \check{C} TOF gas \check{C} | glass \check{C} Fitch \check{C} gas \check{C} | glass \check{C} quartz \check{C} gas \check{C} | quartz \check{C} gas \check{C} Fitch \check{C} |
| P_p (GeV/c) | 0.724 | | | 0.822 | 1.00 | 1.45 | 1.97 | |
| p (\bar{p}) | TOF dE/dX | | TOF dE/dX Fitch \check{C} | TOF dE/dX Fitch \check{C} quartz \check{C} | Fitch \check{C} glass \check{C} quartz \check{C} gas \check{C} | Fitch \check{C} quartz \check{C} gas \check{C} | glass \check{C} quartz \check{C} gas \check{C} | |

$[(\Delta p/p) \Delta \cos\theta \Delta\phi \Delta Z_B]$ is the acceptance of the spectrometer at a given momentum-angle setting for a given particle species, θ = polar angle, ϕ = azimuthal angle, ΔZ_B = effective length of hydrogen target along beam direction, ρ = target density, N_B = number of protons incident on the liquid-hydrogen target, and η = the product of various corrections such as the computer dead-time, the particle decay in flight, the nuclear absorption correction, the track reconstruction efficiency, and the skewing of the mean momentum within the acceptance of the spectrometer.

The Monte Carlo simulation which was used to determine the acceptance of the spectrometer included various experimental effects such as multiple scattering in the hydrogen target, scintillation counters, and MWPC's. All the apertures of the magnet and MWPC's were included in the Monte Carlo program. The Monte Carlo "events" were reconstructed and the target and $\Delta p/p$ distributions were compared with the data giving good agreement. A study of the aperture-determining cuts was made by computing the invariant cross sections for tight chamber cuts versus the cross sections for loose chamber cuts. These cross sections agreed to within 3%.

The nuclear-absorption corrections were performed by using the measured π^\pm , K^\pm , p , and \bar{p} inelastic cross sections as a function of energy.¹¹ In the worst case, these corrections were $\approx 50\%$, but were typically $\leq 30\%$. The decay correction for π^\pm was typically $\approx 10\%$, but for K^\pm this correction was typically $\approx 50\%$.

The incident beam flux was determined by four calibrated secondary-emission monitors (SEM). One SEM was located in the p -West pretarget area upstream of the hydrogen target so that its performance was unaffected by the configuration of the target. The other SEM's were downstream of the liquid-hydrogen target. The SEM's were calibrated by two beam toroids¹² which were calibrated against a constant current source. The SEM calibration by the toroids was performed at 100 and 400 GeV and was checked with a foil activation calibration. The relative uncertainty in this calibration was approximately $\pm 6\%$. The calibration was found to be 14% different between 100 and 400 GeV. The SEM calibration at 200 GeV was determined by a linear interpolation between the measured values at 100 and 400 GeV.

Another measurement of the incident beam intensity was made by a large-angle scintillation-counter telescope. This telescope also served as a monitor of the beam-spill-time structure and independently determined the computer dead time.

To correct for the skewing of the data within the acceptance of the spectrometer, the mean

observed momentum for each spectrometer setting was used in conjunction with the p_\perp and x_R dependencies of the invariant cross sections from a previous data compilation by Taylor *et al.*⁵ This correction affected only the large $x_R \geq 0.75$ data and was typically less than a factor of 2.

Data were taken beyond the kinematic boundary for a free nucleon target to study target associated backgrounds due to secondary processes. The ratio of the invariant cross section at $x_R \sim 1.2$ to that at $x_R \sim 0.9$ was typically $\leq 40\%$ for $p_\perp \sim 1.5$ GeV/c and rapidly decreased with decreasing p_\perp and was neglectable below $p_\perp = 1.0$ GeV/c. Thus only the data at the highest three p_\perp values were corrected for this background by smoothly extrapolating the background cross sections measured above $x_R = 1.0$ into the physical range $x_R < 1$.

Checks were performed on the beam rate dependence by measuring the elastic p - p cross section at various incident proton beam intensities. These studies showed that the measured elastic cross section had no systematic rate dependence and was stable to within $\pm 7\%$ over the factor of 20 in beam intensity employed in the experiment.

THE RESULTS

We shall present the measured invariant cross sections for the reactions $p+p \rightarrow \pi^\pm$, K^\pm , p , or $\bar{p} + X$ in terms of the x_R distributions for a fixed value of p_\perp and the p_\perp distributions of the factorized cross sections. The π^+/π^- , K^+/K^- , and π^\pm/K^\pm particle ratios are discussed and compared with data at higher p_\perp .

A. The x_R distributions

The invariant cross sections for fixed p_\perp as a function of x_R for each of the three incident energies are shown in Fig. 5. Only the statistical errors have been plotted. The estimated $\pm 7\%$ overall normalization errors (based on the reproducibility of the data) have not been included.¹³ The increase of the minimum value of x_R which is plotted as p_\perp increases is due to the upper momentum cutoff of the spectrometer ($p \leq 2.4$ GeV/c) (see Fig. 4). Typical x_R bin widths are $\Delta x_R/x_R \leq 10\%$ full width (FW). We conclude within the estimated normalization errors that the invariant cross sections for $p+p \rightarrow \pi^\pm$, K^\pm , p , or $\bar{p} + X$ scale for fixed p_\perp and x_R over the entire kinematic range of this experiment from 100 to 400 GeV ($\sqrt{s} = 13.8$ to 27.4 GeV). By this scaling behavior we mean that the invariant cross sections for fixed p_\perp and x_R are independent of \sqrt{s} .

To conveniently summarize the ~ 500 data points¹⁴

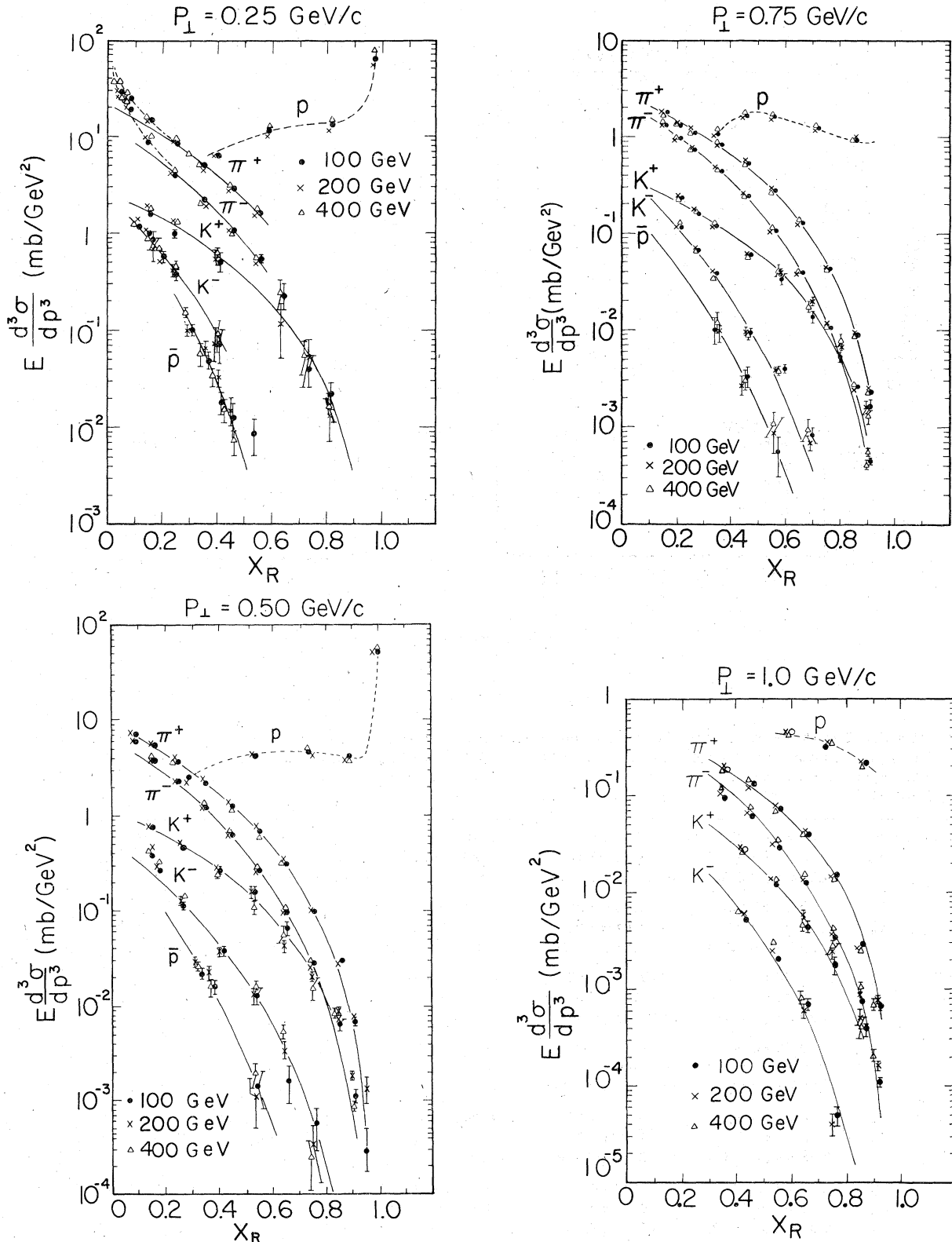


FIG. 5. The invariant cross sections for $p+p \rightarrow \pi^{\pm}, K^{\pm}, p$, or $\bar{p}+X$ are shown for various fixed values of p_{\perp} . The solid lines are the results of the minimum- χ^2 fits given in Table III. The dotted lines through the proton and pion data are to guide the eye.

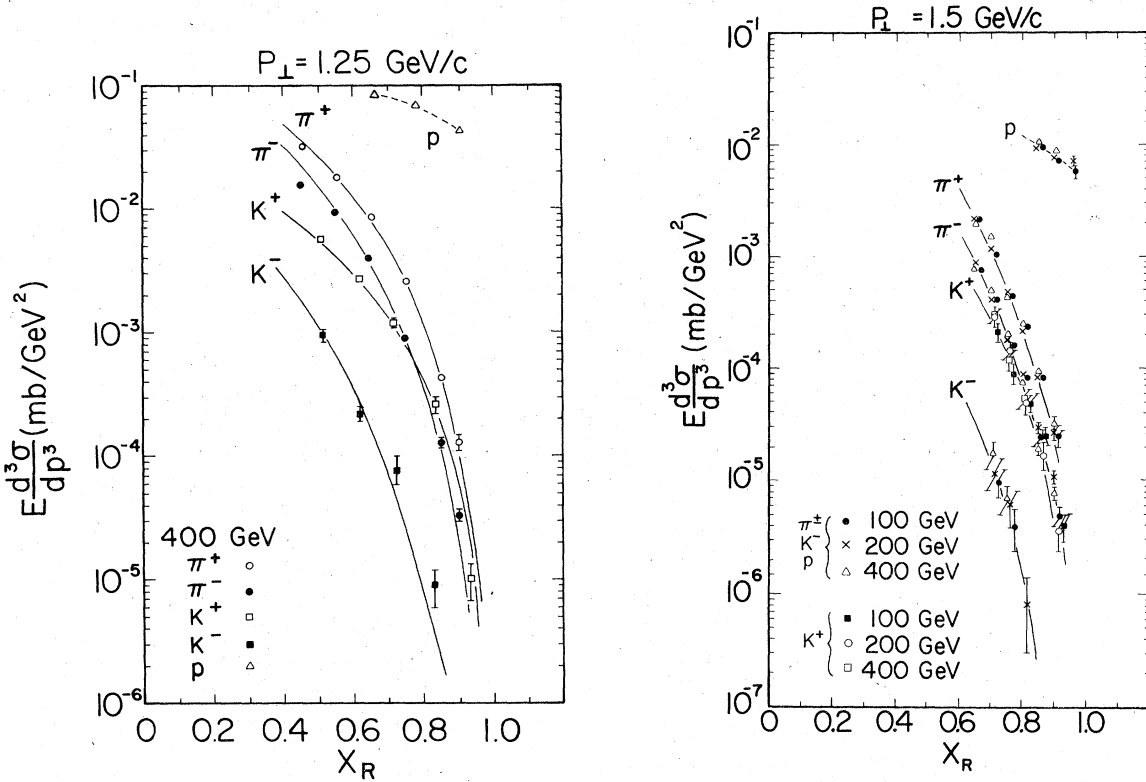


FIG. 5 (continued)

TABLE III. The fitted parameters for the x_R dependence of the invariant cross sections in the reaction $p+p \rightarrow h+X$ for fixed p_\perp are shown. The fit function used was $E(d\sigma/dp^3)(p+p \rightarrow h+X)|_{p_\perp=\text{constant}} = B_h(1-x_R)^{n_h}$.

| p_\perp (GeV/c) | | π^+ | π^- | K^+ | K^- | \bar{p} |
|-------------------|-------|---------------------------------|---------------------------------|-------------------------------|-------------------------------|-----------------------------------|
| 0.25 | B_h | 20.6 ± 0.9 | 12.8 ± 1.0 | 2.72 ± 0.32 | 2.58 ± 0.32 | 3.59 ± 1.16 |
| | N_h | 3.23 ± 0.08 | 4.04 ± 0.15 | 2.96 ± 0.21 | 6.69 ± 0.45 | 9.78 ± 0.69 |
| | | $(0.25 \leq x_R \leq 0.56)$ | $(0.25 \leq x_R \leq 0.56)$ | $(0.24 \leq x_R \leq 0.82)$ | $(0.20 \leq x_R \leq 0.82)$ | $(0.28 \leq x_R \leq 0.54)$ |
| 0.50 | B_h | 9.46 ± 0.35 | 6.85 ± 0.29 | 1.21 ± 0.16 | 0.56 ± 0.05 | 0.52 ± 0.09 |
| | N_h | 3.29 ± 0.07 | 4.04 ± 0.06 | 2.89 ± 0.16 | 4.96 ± 0.20 | 7.60 ± 0.37 |
| | | $(0.25 \leq x_R \leq 0.76)$ | $(0.25 \leq x_R \leq 0.76)$ | $(0.40 \leq x_R \leq 0.76)$ | $(0.26 \leq x_R \leq 0.76)$ | $(0.31 \leq x_R \leq 0.55)$ |
| 0.75 | B_h | 2.83 ± 0.10 | 2.33 ± 0.03 | 0.40 ± 0.02 | 0.44 ± 0.05 | 0.22 ± 0.05 |
| | N_h | 2.94 ± 0.05 | 3.82 ± 0.02 | 2.77 ± 0.08 | 5.97 ± 0.26 | 7.0 ± 0.4 |
| | | $(0.20 \leq x_R \leq 0.76)$ | $(0.20 \leq x_R \leq 0.76)$ | $(0.20 \leq x_R \leq 0.80)$ | $(0.20 \leq x_R \leq 0.70)$ | $(0.34 \leq x_R \leq 0.58)$ |
| 1.00 | B_h | 0.72 ± 0.04 | 0.55 ± 0.04 | 0.15 ± 0.03 | 0.09 ± 0.02 | |
| | N_h | 2.86 ± 0.07 | 3.52 ± 0.08 | 3.20 ± 0.21 | 4.89 ± 0.34 | |
| | | $(0.35 \leq x_R \leq 0.86)$ | $(0.35 \leq x_R \leq 0.76)$ | $(0.42 \leq x_R \leq 0.76)$ | $(0.42 \leq x_R \leq 0.77)$ | |
| 1.25 ^a | B_h | 0.28 ± 0.04 | 0.27 ± 0.04 | 0.04 ± 0.01 | 0.04 ± 0.01 | |
| | N_h | 3.4 ± 0.1 | 4.1 ± 0.2 | 2.83 ± 0.16 | 5.2 ± 0.8 | |
| | | $(0.55 \leq x_R \leq 0.85)$ | $(0.45 \leq x_R \leq 0.85)$ | $(0.62 \leq x_R \leq 0.83)$ | $(0.50 \leq x_R \leq 0.83)$ | |
| 1.50 | B_h | 0.08 ± 0.02 | 0.08 ± 0.02 | 0.013 ± 0.004 | 0.01 ± 0.01 | |
| | N_h | 3.6 ± 0.2 | 4.1 ± 0.2 | 3.2 ± 0.2 | 5.4 ± 0.7 | |
| | | $(0.35 \leq x_R \leq 0.92)$ | $(0.65 \leq x_R \leq 0.92)$ | $(0.70 \leq x_R \leq 0.93)$ | $(0.70 \leq x_R \leq 0.82)$ | |
| Average | | $\bar{n}_{\pi^+} = 3.2 \pm 0.3$ | $\bar{n}_{\pi^-} = 3.9 \pm 0.2$ | $\bar{n}_{K^+} = 3.0 \pm 0.2$ | $\bar{n}_{K^-} = 5.5 \pm 0.7$ | $\bar{n}_{\bar{p}} = 8.1 \pm 1.4$ |

^aOnly 400-GeV data have been taken at this transverse momentum.

of this experiment and to compare the radial dependencies of various particle species, we have performed minimum- χ^2 fits to the x_R dependence of the invariant cross sections in the range $0.2 \leq x_R \leq 0.8$ for fixed p_\perp . The form used was

$$E \frac{d\sigma}{dp^3}(p+p \rightarrow h+X) \Big|_{p_\perp=\text{constant}} = B_h(1-x_R)^{n_h}, \quad (2)$$

where B_h and n_h are free parameters. The results are presented in Table III. We find agreement with the fitted parameters of an earlier data compilation by Taylor *et al.*⁵ of the data at lower and higher energies. We conclude: The invariant cross sections (with the exclusion of $p+p \rightarrow p+X$) for fixed p_\perp and $x_R \geq 0.2$ follow a power law in $(1-x_R)$ to a good approximation. For the π^\pm invariant cross sections, $x_R < 0.2$ and $p_\perp \leq 0.5$ GeV/c, there is some enhancement over this power-law behavior. In addition, there is evidence that the π^+ and π^- invariant cross sections converge as $x_R \rightarrow 0$ in this low- $p_\perp \leq 0.5$ -GeV/c region. However, over the range $0.25 \leq p_\perp \leq 1.5$ GeV/c and $0.2 \leq x_R \leq 0.8$, the values of n_h determined by these fits are roughly constant. We notice that π^+ and K^+ have roughly the same value of n_h , whereas the corresponding values for π^- , K^- , and \bar{p} are progressively larger. The power n_h of the radial scaling dependence is then correlated with the quantum-number requirements for particle production, namely the power n_h increases with increasing quantum-number conservation requirements.¹⁵

B. The p_\perp distributions

Since the values of n_h determined by the fits of the invariant cross sections for fixed p_\perp are roughly constant, we have plotted the factorized invariant cross sections for the inclusive production of a hadron h ,

$$g_h(p_\perp) = \frac{E(d\sigma/dp^3)(p_\perp, x_R)}{(1-x_R)^{\bar{n}_h}}, \quad (3)$$

where \bar{n}_h is the average value of n_h over the range $0.25 \leq p_\perp \leq 1.5$ GeV/c given in Table III. The factorized p_\perp distributions for $p+p \rightarrow h+X$, where

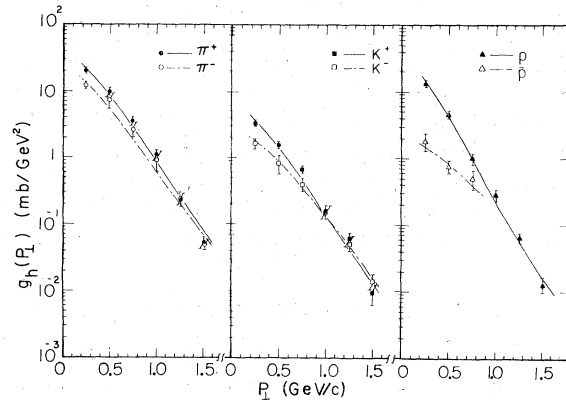


FIG. 6. The factorized p_\perp distributions are shown. The error bars represent the violations to exact factorization. The lines are the fits given in Table IV.

$h = \pi^\pm, K^\pm, p$, or \bar{p} for $x_R \geq 0.2$, are shown in Fig. 6. It is well established that the invariant cross sections for fixed x_R at large p_\perp show a power-law dependence $\sim 1/p_\perp^3$ which suggests that the scattering of pointlike constituents is responsible for the production of hadrons.^{1,2} It is evident from Fig. 6 that this simple behaviour does not extend to the lower values of p_\perp measured in this experiment.

Fits to the p_\perp dependences $g_h(p_\perp)$ of the form

$$g_h(p_\perp) = \frac{A_h}{(1+p_\perp^2/m_h^2)^2}, \quad (4)$$

with A_h and m_h^2 as free parameters, have been performed. The results are presented in Table IV. The fits require that at high p_\perp , $g_h(p_\perp) \propto 1/p_\perp^3$ and are therefore consistent with the observed behavior in that region but account for the observed deviations from the power law at low p_\perp by including the "mass" term m_h^2 . The values of m_h^2 for π^\pm, K^\pm are roughly equal ~ 0.7 (GeV/c)², but K^- and \bar{p} require larger m_h^2 values of 0.9 and ~ 1.2 (GeV/c)² respectively. For protons, $m_h^2 \sim 0.4$ (GeV/c)². In the latter case the p_\perp dependence for $p+p \rightarrow p+X$ has been computed at $x_R = 0.8$ since the x_R dependence is rather complicated and no factoriza-

TABLE IV. Tabulated are the fitted parameters of the factorized p_\perp dependences. The function used was $g_h(p_\perp) = A_h/(1+p_\perp^2/m_h^2)^2$. For protons only the function $g_h(p_\perp)$ for $x_R = 0.8$ is given.

| | π^+ | π^- | K^+ | K^- | p | \bar{p} |
|---------------------------------|----------------|-----------------|-----------------|---------------|-----------------|---------------|
| A_h [(mb/GeV) ²] | 30.2 ± 0.5 | 17.4 ± 0.4 | 5.3 ± 0.5 | 2.3 ± 0.5 | 27.0 ± 3.5 | 1.9 ± 0.4 |
| m_h^2 [(GeV/c) ²] | 0.66 ± 0.1 | 0.74 ± 0.01 | 0.64 ± 0.03 | 0.9 ± 0.1 | 0.41 ± 0.02 | 1.2 ± 0.3 |

tion could be performed. The particles π^+ , K^+ (and p) contain valence quarks in common with the colliding protons, whereas K^- and \bar{p} do not. In light of the m_h^2 dependence on the secondary-particle species, it is interesting to speculate that the low- p_\perp behaviour of the invariant cross sections depends on the quark constituents of the secondary particle as well as the quark constituents of the initial particles.

C. The π^+/π^- and K^+/K^- particle ratios

It is of interest to study the particle ratios π^+/π^- and K^+/K^- versus x_R for both small- p_\perp and large- p_\perp data. The low- p_\perp region is characterized by long-range interactions and is often described by Regge or diffractive scattering. The high- p_\perp region is characterized by short-range interactions and can be described by the quark-parton model. Therefore these two kinematic regions are not related in any obvious way. Recently, however, there have been theoretical attempts¹⁶ to unify these two regions by applying the quark-parton model to the low- p_\perp region.

In Fig. 7 we have plotted the invariant cross-section ratios as a function x_R for both the data of this experiment for small p_\perp ($0.25 \leq p_\perp \leq 1.5$ GeV/c are averaged together) in the fragmentation region and the data of Antreasyan *et al.*¹⁷ at large p_\perp ($0.77 \leq p_\perp \leq 7.67$ GeV/c) at 90° in the c.m. frame. It is evident from Fig. 7 that the particle ratios in these two different kinematic regions are in remarkable agreement, indicating that the particle ratios are independent of p_\perp and that the correct scaling variable to use in both kinematic regions is the radial variable x_R . The lack of any p_\perp dependence in these particle ratios suggests that the ratios are uniquely dependent on the quantum-number requirements for particle production.

The predictions of the quark-quark elastic-scattering model of Field and Feynman¹ at 90° in the c.m. frame are compared with the particle ratio data in Fig. 7. We find that the theoretical predictions are in good agreement with the data of π^+/π^- and K^+/K^- for $x_R \leq 0.6$. However, for the π^+/π^- ratio at values of $x_R \geq 0.6$, there is an indication that the data lie below the theory. Ochs¹⁶ has observed that the π^+/π^- ratio measured in p - p collisions is independent of p_\perp and closely follows the $u(x)/d(x)$ ratio, where $u(x)$ and $d(x)$ are the number of up quarks and down quarks respectively in a proton between a momentum fraction x and $x+dx$ and are determined by deep-inelastic lepton-scattering experiments. This remarkable similarity of the π^+/π^- ratio and the $u(x)/d(x)$ ratio suggests that π^+ and π^- meson cross

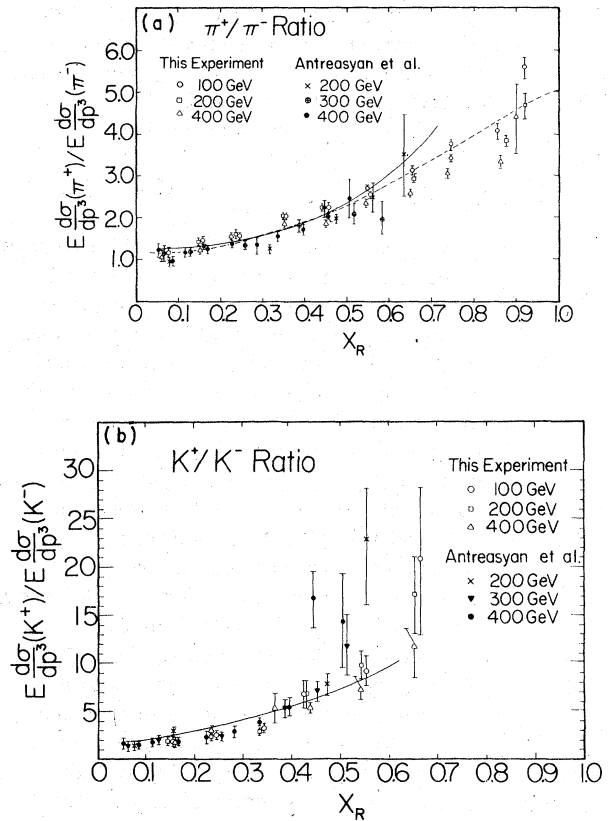


FIG. 7. The particle ratios (a) π^+/π^- and (b) K^+/K^- from the data of this experiment and that of Ref. 17 are plotted versus x_R . For the K^+/K^- ratio, the data at $x_R \geq 0.6$ from Ref. 17 have not been plotted since the error bars are very large. The smooth lines are the predictions of Field and Feynman (Ref. 1). The dotted line in Fig. 7(a) is the calculation of Duke and Taylor (Ref. 19).

sections in high-energy p - p collisions are determined by the u and d valence-quark distributions in the proton. In addition Farrar and Jackson¹⁸ have discussed a quark-vector-gluon model in which the helicity of the fast quark ($x_R \rightarrow 1$) is the same as that of the proton which implies that u/d quark ratio approaches 5 as $x_R \rightarrow 1$. This leads to the π^+/π^- ratio $\rightarrow 5$ since it is determined by this quark ratio. From Fig. 7 we see that this prediction is in good agreement with the data. The K^+/K^- ratio on the other hand tends to ∞ as $x_R \rightarrow 1$ since the K^- contains no valence quarks in common with the incident protons.

The theoretical predictions of Field and Feynman¹ and Farrar and Jackson¹⁸ are claimed to be valid for short-distance behavior. But the data indicate that the particle ratios π^+/π^- and

K^+/K^- are remarkably insensitive to transverse momentum implying that these particle ratios are therefore insensitive to the range of the interaction. It is therefore tempting to infer from the data that the alignment of the spin of the proton and the spin of the leading valence quark at large x_R is a general phenomenon of hadron interactions.

Das and Hwa¹⁶ have noted the empirical observation of Ochs,¹⁶ and have developed a model based on proton fragmentation into quarks followed by quark-antiquark recombination. They obtain reasonable agreement with the observed x_R dependence of π^\pm and K^\pm inclusive production in p - p collisions. In Fig. 7(a) we have plotted the prediction of this model¹⁹ which we see is in good agreement with the data.

D. The π^\pm/K^\pm ratios

The π^\pm/K^\pm ratios are less amenable to theoretical interpretation than the particle/antiparticle ratios discussed above since we must contend with possible mass effects. Nevertheless it is interesting to examine the π^\pm/K^\pm ratios as a function of x_R in both the small- and the large- p_\perp region.

In Fig. 8 are shown the π^+/K^+ and the π^-/K^- ratios of this experiment (averaged over $p_\perp \leq 1.5$ GeV/ c) and that of Antreasyan *et al.*¹⁷ at high $p_\perp \leq 7.7$ GeV/ c . We notice that the particle ratios at low p_\perp are roughly three times larger than those at high p_\perp . This p_\perp dependence is not difficult to understand in view of the different p_\perp dependence of pions and kaons.

However, the x_R dependence of the π^\pm/K^\pm ratios is roughly the same in these two kinematic regions. The π^+/K^+ ratio is very slowly decreasing with increasing x_R for $x_R > 0.1$ whereas the π^-/K^- ratio is rapidly increasing with increasing x_R for $x_R > 0.2$. This behavior can be qualitatively understood in terms of the valence quark structure of the π^\pm, K^\pm mesons.²⁰ Consider the π^+/K^+ ratio. Both the π^+ and K^+ contain a u valence quark which comes from the u valence quark of the fragmenting target proton (we are in the target-fragmentation region). We would therefore expect the π^+/K^+ ratio to be roughly constant. On the other hand for the π^-/K^- ratio, the π^- is a d, \bar{u} state and the K^- is a s, \bar{u} state. The d valence quark of the π^- is the d valence quark of the fragmenting target proton, but both the valence quarks of the K^- must come from the sea. We expect the π^-/K^- ratio to increase rapidly with increasing x_R since it is generally understood that the sea-quark x distributions are steeply falling with increasing x . These are the qualitative effects which are observed.

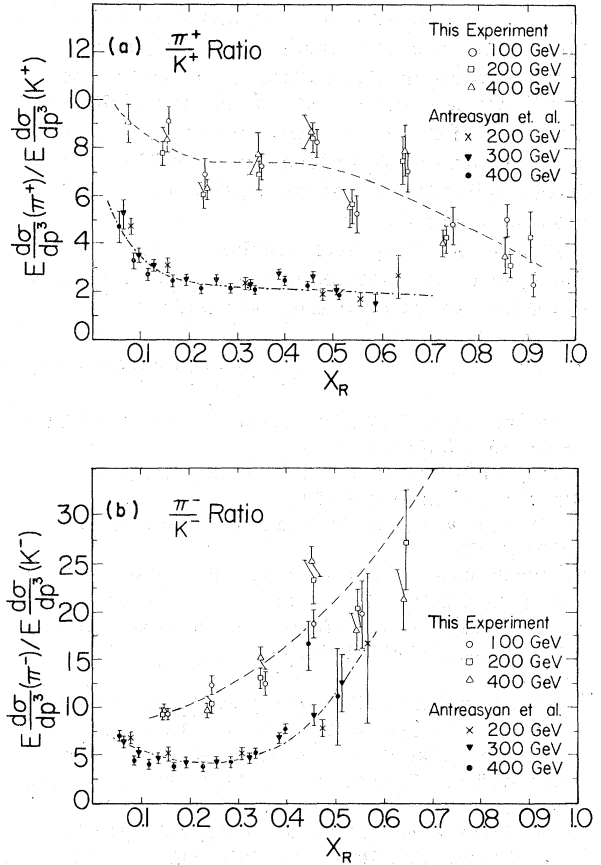


FIG. 8. (a) The π^+/K^+ ratio from data of this experiment and that of Antreasyan *et al.* (Ref. 17). The dotted lines are to guide the eye. The low value of this ratio at $x_R = 0.55$ is probably not significant and is due to our overall normalization errors. (b) The π^-/K^- ratios from this experiment and Ref. 17 are shown.

CONCLUSIONS

The single-particle inclusive cross sections for fixed p_\perp ($0.25 \leq p_\perp \leq 1.50$ GeV/ c) and x_R ($0.05 \leq x_R \leq 0.9$) scale from 100 to 400 GeV.²¹ The radial scaling distributions for fixed p_\perp can be represented by the power law $B_h(1-x_R)^{n_h}$, where the values of n_h are species dependent, but are roughly independent of p_\perp for $0.25 \leq p_\perp \leq 1.5$ GeV/ c .

The factorized p_\perp distributions are consistent with a power law $A_h/(1+p_\perp^2/m_h^2)^4$. The rare particles K^- and \bar{p} have a less steep p_\perp dependence at very low p_\perp than the more copious particles π^+, K^+, p . This suggests that the low- p_\perp behavior of single-particle inclusive cross sections depends on the constituent structure of the participating hadrons.

The particle ratios π^+/π^- and K^+/K^- are re-

markably independent of the transverse momentum. This behavior suggests that the particle ratios depend on the constituent makeup of the participating hadrons, but not on the specific dynamics of the particle production. The π^{\pm}/K^{\pm} ratios show a p_{\perp} dependence because of the different p_{\perp} dependence of the cross sections for pions and kaons.

Finally, single-particle inclusive reactions at low p_{\perp} and high energies present a rich territory to explore the quark-parton structure of hadrons.

ACKNOWLEDGMENTS

We would like to thank M. Atac, D. C. Carey, T. Collins, A. Roberts, and J. Sauer for their help in the early phases of the experiment, R. Brock and P. Neeson for their help in the data taking and preliminary data analysis and D. Burandt, R. Olsen, B. Cox, C. T. Murphy, and the personnel of the Proton Laboratory for their excellent technical support. Conversations with D. W. Duke are gratefully acknowledged.

*Present address: Stanford Linear Accelerator Center, Stanford, California 94305.

†Present address: Lawrence Berkeley Laboratory, Berkeley, California 94720.

¹R. D. Field and R. P. Feynman, Phys. Rev. D 15, 2590 (1977).

²R. Blankenbecler, S. J. Brodsky, and J. Gunion, Phys. Rev. D 12, 3469 (1975).

³A preliminary version of this work has been published: J. R. Johnson *et al.*, Phys. Rev. Lett. 39, 1173 (1977).

⁴D. C. Carey *et al.*, Phys. Rev. Lett. 33, 327 (1974); D. C. Carey *et al.*, *ibid.* 33, 330 (1974); D. C. Carey *et al.*, Fermilab Report No. 75/20-EXP, 1975 (unpublished); D. C. Carey *et al.*, Phys. Rev. D 14, 1196 (1976).

⁵F. E. Taylor *et al.*, Phys. Rev. D 14, 1217 (1976).

⁶P. F. Cooper, Jr., Report No. CEA-TM-74, 1961 (unpublished).

⁷T. Collins, private communication.

⁸K. L. Brown *et al.*, Report No. NAL-91, 1974 (unpublished).

⁹P. Neeson, thesis, Northern Illinois University, 1976 (unpublished).

¹⁰Jerry Friedman and Roger Chaffee, SLAC Report No. SLAC-CGTM No. 136 (unpublished).

¹¹The inelastic cross sections were obtained from the following: B. W. Alladyce *et al.*, Nucl. Phys. A209, 1 (1973); D. V. Bugg *et al.*, Phys. Rev. 168, 1466 (1968); R. J. Abrams *et al.*, Phys. Rev. D 4, 3235

(1971); M. M. Sternheim and R. R. Silbar, Annu. Rev. Nucl. Sci. 24, 249 (1974); J. Sandinos and C. Wilkin, *ibid.* 24, 341 (1974).

¹²C. Kerns, IEEE Trans. Nucl. Sci. NS-20, 204 (1973).

¹³The absolute normalization uncertainty is difficult to estimate. However, from the $\Delta p/p = \pm 2\%$ spectrometer momentum-calibration uncertainty, normalization errors as large as $\pm 40\%$ can result at large p_{\perp} and large x_R .

¹⁴The complete data of this experiment are given in AIP document No. PAPS PRVDA-17-1292-21. Order by PAPS number and journal reference from American Institute of Physics, Physics Auxiliary Publication Service, 335 East 45th Street, New York, New York, 10017. The price is \$1.50 for microfiche, or \$5 for photocopies.

¹⁵S. J. Brodsky and J. F. Gunion, Phys. Rev. D 17, 848 (1978).

¹⁶K. P. Das and Rudolph C. Hwa, Phys. Lett. 68B, 459 (1977); W. Ochs, Nucl. Phys. B118, 397 (1977).

¹⁷D. Antreasyan *et al.*, Phys. Rev. Lett. 38, 112 (1977); 38, 115 (1977).

¹⁸G. R. Farrar and D. R. Jackson, Phys. Rev. Lett. 35, 1416 (1975).

¹⁹D. W. Duke and F. E. Taylor, Phys. Rev. D (to be published).

²⁰We argue in the context of the model of Das and Hwa (Ref. 16).

²¹See Ref. 5 for a comparison of radial scaling of lower and higher energies than covered by this experiment.